Flexibility of the petunia strigolactone receptor DAD2 promotes its interaction with signaling partners

Received for publication, October 16, 2019, and in revised form, February 13, 2020 Published, Papers in Press, February 17, 2020, DOI 10.1074/jbc.RA119.011509

Hui Wen Lee[‡§1,2], Prachi Sharma[‡§1,3], Bart J. Janssen[‡], Revel S. M. Drummond[‡], Zhiwei Luo[‡], Cyril Hamiaux[‡], Thomas Collier[¶], Jane R. Allison[§‖**], Richard D. Newcomb[‡§], and Kimberley C. Snowden[‡4]

*From the [‡]The New Zealand Institute for Plant & Food Research Limited, Auckland, New Zealand, the [§]School of Biological Sciences, University of Auckland, Auckland, New Zealand, the [¶]School of Natural and Computational Sciences, Massey University Albany, Auckland, New Zealand, the [‖]Digital Life Institute & Maurice Wilkins Centre for Molecular Biodiscovery, University of Auckland, Auckland, New Zealand, and the **Biomolecular Interaction Centre, University of Canterbury, Christchurch, New Zealand*

Edited by Joseph M. Jez

Strigolactones (SLs) are terpenoid-derived plant hormones that regulate various developmental processes, particularly shoot branching, root development, and leaf senescence. The SL receptor has an unusual mode of action. Upon binding SL, it hydrolyzes the hormone, and then covalently binds one of the hydrolytic products. These initial events enable the SL receptor DAD2 (in petunia) to interact with the F-box protein PhMAX2A of the Skp-Cullin-F-box (SCF) complex and/or a repressor of SL signaling, PhD53A. However, it remains unclear how binding and hydrolysis structurally alters the SL receptor to enable its engagement with signaling partners. Here, we used mutagenesis to alter DAD2 and affect SL hydrolysis or DAD2's ability to interact with its signaling partners. We identified three DAD2 variants whose hydrolytic activity had been separated from the receptor's interactions with PhMAX2A or PhD53A. Two variants, DAD2^{N242I} and DAD2^{F135A}, having substitutions in the core α/β hydrolase-fold domain and the hairpin, exhibited hormone-independent interactions with PhMAX2A and PhD53A, respectively. Conversely, the DAD2^{D166A} variant could not interact with PhMAX2A in the presence of SL, but its interaction with PhD53A remained unaffected. Structural analyses of DAD2^{N242I} and DAD2^{D166A} revealed only small differences compared with the structure of the WT receptor. Results of molecular dynamics simulations of the DAD2^{N242I} structure suggested that increased flexibility is a likely cause for its SL-independent interaction with PhMAX2A. Our results suggest that PhMAX2A and PhD53A have distinct binding sites on the SL receptor and that its flexibility is a major determinant of its interactions with these two downstream regulators.

This work was supported by the Marsden Fund from Royal Society Te Apārangi Contract PAF1301, by Plant and Food Research, and Rutherford Discovery Fellowship Grant 15-MAU-001 (to J. R. A.). The authors declare that they have no conflicts of interest with the contents of this article.

This article contains Figs. S1–S12, Movie S1, and Table S1.

The atomic coordinates and structure factors (codes 6UH8 and 6UH9) have been deposited in the Protein Data Bank (http://wwpdb.org/).

[1] Both authors contributed equally to this work.

[2] Present address: Plant Health and Environment Laboratory, Ministry for Primary Industries, Auckland, New Zealand.

[3] Present address: Dept. of Molecular Medicine and Pathology, University of Auckland, Auckland, New Zealand.

[4] To whom correspondence should be addressed: The New Zealand Institute for Plant & Food Research Limited, Auckland 1142, New Zealand. Tel.: 64-9-925-7180; E-mail: kimberley.snowden@plantandfood.co.nz.

Strigolactones (SLs)[5] are a group of terpenoid-derived plant hormones, characterized by a butenolide ring linked to a tricyclic lactone by an enol–ether bridge. They were initially identified as exogenous signals that promote the germination of parasitic weeds, as well as symbiosis between host plants and arbuscular mycorrhizal fungi (1–3). In plants, SLs regulate various developmental processes, particularly shoot branching, root development, and leaf senescence (4–9).

The SL signal is perceived by an α/β hydrolase-fold protein that possesses a canonical Ser-His-Asp catalytic triad in its active site cavity (10). Orthologs of the SL receptor have been identified from a number of species, including petunia (DECREASED APICAL DOMINANCE 2; DAD2 (10)), rice (DWARF14; OsD14 (11, 12)), *Arabidopsis* (*Arabidopsis thaliana* D14; AtD14 (13)), and pea (RAMOSUS3; RMS3 (14)). The catalytic triad allows the SL receptor to slowly hydrolyze the SL molecule at the enol–ether linkage, resulting in the generation of a tricyclic lactone (ABC-ring) and a butenolide product (D-ring (10, 12, 14, 15)). SL hydrolysis by the SL receptor leads to the covalent modification of the catalytic histidine residue as shown for AtD14, OsD14, and RMS3 (14, 16, 17).

Numerous studies have shown that the receptor has a lower melting temperature (T_m) in the presence of SL (10, 14, 18–20). In response to SL, the receptor interacts with an F-box protein of the Skp1-Cullin1-F-box (SCF) ubiquitin ligase complex: petunia (MORE AXILLARY GROWTH 2A, PhMAX2A); *Arabidopsis* (MAX2); rice (DWARF3, D3) (10, 16, 19)) and the repressors of SL signaling: petunia (PhD53A); rice (DWARF53, D53); *Arabidopsis* (Suppressor of MAX2-Like, SMXL 6/7/8) (21–25). The interaction between the receptor, SCF ubiquitin ligase complex, and the SL repressor protein, leads to degradation of the repressor protein in an ubiquitin-dependent manner via the 26S proteasomal pathway, resulting in the activation of the SL signaling cascade (26).

Several research groups have crystallized the SL receptor in the presence of SL and SL-intermediates, with none of these

[5] The abbreviations used are: SL, strigolactone; DAD2, Decreased Apical Dominance 2; MAX2A, More Axillary Growth 2A; DSF, differential scanning fluorimetry; YLG, yoshimulactone green; MD, molecular dynamics; RMSF, root-mean-square fluctuation; Bicine, *N*,*N*-bis(2-hydroxyethyl)glycine; PDB, Protein Data Bank; MBP, maltose-binding protein; RMSD, root-mean-square deviation; β-gal, β-galactosidase.

ligand-associated receptor structures showing a substantial change in conformation compared with the apo-receptor structures (12, 15, 19, 27). In 2015, Zhao *et al.* (19) reported that the OsD14 receptor, in the presence of the synthetic SL analogue, GR24, showed a similar deuterium exchange rate as that observed for the receptor alone, which is consistent with the structural evidence of minimal conformational change. The OsD14 receptor does, however, show increased deuterium exchange in the presence of both GR24 and the rice F-box protein D3. These results suggested that the SL receptor undergoes conformational change in the presence of both SL and the F-box protein and that binding of the SL ligand alone may not lead to a conformational change.

Consistent with the findings for the rice receptor of Zhao *et al.* (19), structural characterization of the *Arabidopsis* receptor AtD14 in complex with the F-box protein D3 and ASK1 (ARABIDOPSIS SKP1-LIKE1, another component of the SCF complex and required for efficient expression of the F-box protein) showed that AtD14 underwent a conformational change in its four-helix-lid domain (Fig. S1) upon interaction with D3. A SL hydrolysis intermediate called CLIM (Covalently-Linked Intermediate Molecule, composed of the D-ring from the SL ligand) was proposed to be trapped within the cavity of the bound AtD14 receptor and covalently linked to the catalytic His and Ser residues (16). Based on the structure of the AtD14-D3-ASK1 protein complex, it was proposed that SL hydrolysis and/or binding of the D-ring to the catalytic histidine residue of AtD14 play a role in generation of the active conformation of AtD14, allowing interaction with D3 (16). Using MS, Yao *et al.* (16) showed that the D-ring covalently binds to AtD14 both *in vitro* and *in vivo*, although the attachment was detected only on the catalytic His residue of the AtD14 receptor (16). A similar modification was also detected on the catalytic His residue of the pea SL receptor, RMS3, after it was incubated with GR24 (14). These findings suggest a possible role of D-ring binding in the formation of the active conformation of the SL receptor for interaction with the SCF complex.

In contrast with the hydrolysis-dependent mechanism of SL signaling discussed above, recent work by Seto *et al.* (28) suggests a hydrolysis-independent mechanism of SL signaling. Based on their observations of altered T_m of the AtD14 receptor in the presence of a range of different ligands over time, the authors suggested that an intact SL molecule probably leads to or induces the active signaling state of the AtD14 receptor (28). The authors further showed that a catalytic amino acid mutant, $AtD14^{D218A}$, defective in SL hydrolysis, could bind an intact SL molecule with high affinity and cause a small T_m change. The $AtD14^{D218A}$ mutant, in the presence of SL, could also interact with the MAX2-ASK1 complex and SMXL7 in yeast two-hybrid assays (28). When expressed *in planta*, this mutant could complement the *Atd14-1* knockout mutant but not the *Atd14 max4* (receptor and SL biosynthesis) double mutant (28). These findings led to the hypothesis that SL hydrolysis by D14 is not essential for the initiation of SL signal transduction. In a study conducted by Shabek *et al.* (29), the rice F-box protein D3 was shown to regulate the hydrolytic activity of OsD14 via its C-terminal α-helix, and the authors also proposed that the D3 protein can bind different conformations of the OsD14 receptor (open or closed) via its C-terminal α-helix, suggesting that the F-box protein might be involved in the selection of hydrolysis-dependent or hydrolysis-independent signaling mechanisms by binding the receptor in different conformations.

Despite these advances we still do not completely understand how hydrolysis alters the WT receptor to allow interaction with signaling partners. We know that some mutations can dispense with the requirement for hydrolysis to enable interaction with signaling partners. Here we aimed to use mutagenesis to generate mutants with the ability to interact with the F-box protein PhMAX2A or the target protein PhD53A, even in the absence of hormone. Biochemical and structural analysis of these mutants was undertaken to provide insight into how the receptor becomes capable of interacting with partners, without the need for including a ligand that, in WT, is hydrolyzed during perception.

Results

Mutations on the lid domain and core α/β hydrolase-fold altered interaction with PhMAX2A and PhD53A

To understand the relative contributions of the different functions of the DAD2 SL receptor, we used mutagenesis to identify variants of DAD2 showing changes in interactions with binding partners, and/or altered enzyme activity. Two approaches were used. The first was to use random mutagenesis together with a yeast two-hybrid screen for mutants that could interact with binding partners in the absence of hormone. The other approach was to specifically mutate residues based on their location within the receptor or how well they were conserved in orthologous proteins. Of the mutants generated (Fig. S2 and Fig. 1), $DAD2^{N242I}$, $DAD2^{D166A}$, $DAD2^{F135A}$ were selected for further analysis as these mutants had altered interactions with binding partners. We also included the active site mutant $DAD2^{S96A}$, as well as the $DAD2^{S96A/N242I}$ and $DAD2^{F135A/N242I}$ double mutants (Fig. 1, Figs. S1–S3). The $DAD2^{S96A}$ catalytic site mutant had previously been shown to have lost its hydrolytic activity and also the ability to interact with the F-box protein, PhMAX2A, or to complement the *dad2* mutant background (Fig. 1*A*; also see Ref. 10).

The $DAD2^{N242I}$ mutant was able to interact with PhMAX2A in the absence of GR24 (Fig. 1*A*). This interaction with PhMAX2A in the absence of hormone could still occur even in combination with the active-site mutation ($DAD2^{S96A/N242I}$). In the presence of GR24, the overall interaction level for this double mutant with PhMAX2A was reduced compared with that of $DAD2^{WT}$. The $DAD2^{F135A}$ mutant, similar to $DAD2^{WT}$, could not interact with PhMAX2A in the absence of GR24, although the double mutant $DAD2^{F135A/N242I}$ was able to interact with PhMAX2A in the absence of GR24 (Fig. 1*C*). The $DAD2^{F135A/N242I}$ double mutant also showed a lower level of interaction with PhMAX2A in the presence of GR24, compared with the levels shown in the absence of GR24. The $DAD2^{D166A}$ mutant showed the same baseline interaction as the negative control with PhMAX2A in the absence or presence of GR24 (Fig. 1*B*).

We also investigated the ability of these mutants to interact with the target repressor protein PhD53A. $DAD2^{WT}$ interac-

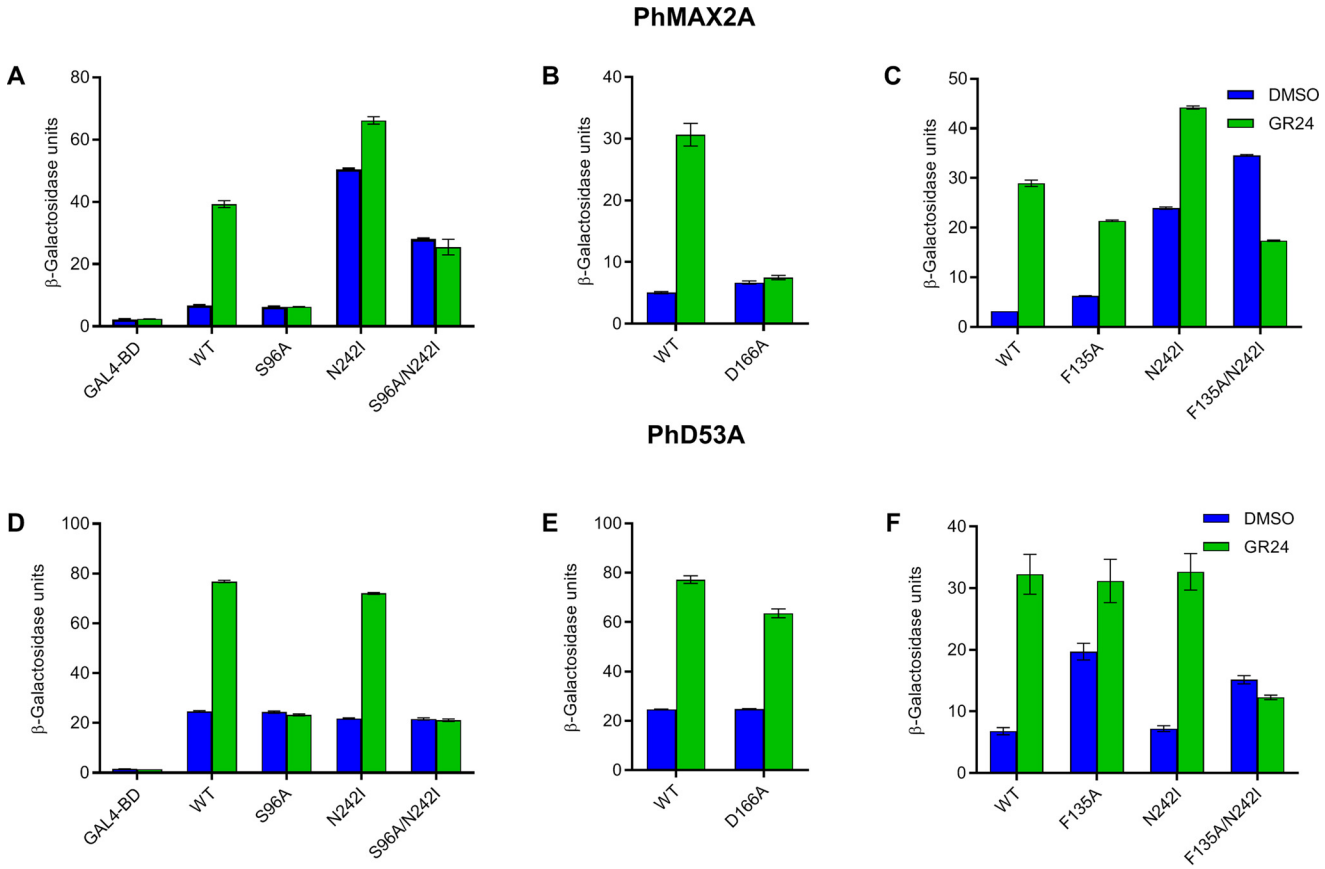

Figure 1. Interaction of DAD2 mutants with PhMAX2A and PhD53A. *A–C*, interaction of DAD2 mutants with PhMAX2A. *D–F*, interaction of DAD2 mutants with PhD53A. Interactions in each figure were quantified in the presence and absence of GR24 (10 μM for *A–C* and 1 μM for *D–F*) using yeast two-hybrid β-gal liquid culture assays. All data shown are mean ± S.E.; $n = 3$ technical replicates. Western blotting analyses confirming the presence of the fusion proteins in yeast are shown in Fig. S3.

tion with PhD53A is induced by GR24 and this interaction is retained by both DAD2^{N242I} and DAD2^{D166A} mutants (Fig. 1, *D* and *E*). The DAD2^{F135A} and DAD2$^{F135A/N242I}$ mutants both showed a strong interaction with PhD53A in the absence of GR24 (Fig. 1*F*). However, DAD2$^{F135A/N242I}$ showed an overall reduced ability to interact with PhD53A in the presence of GR24 compared with DAD2^{WT}. Neither the DAD2^{S96A} nor the DAD2$^{S96A/N242I}$ mutants were able to interact with PhD53A (Fig. 1*D*).

To examine the interaction between DAD2 and PhD53A in the presence of PhMAX2A, we generated yeast expressing all three proteins (Fig. 2). The presence of PhMAX2A reduced the strength of interaction between DAD2^{WT} and PhD53A in the presence of GR24 (Fig. 2). This decrease was also observed for the DAD2 mutants, DAD2^{N242I} and DAD2^{F135A}, but not DAD2^{S96A}, DAD2$^{S96A/N242I}$, and DAD2$^{F135A/N242I}$ (Fig. 2). In the absence of GR24, PhMAX2A enhanced the interaction between DAD2$^{F135A/N242I}$ and PhD53A, and also between DAD2^{N242I} and PhD53A (Fig. 2*B*).

DAD2 mutants have altered melting temperature compared with DAD2^{WT}

We investigated the thermal stability of the DAD2 mutants (DAD2^{F135A}, DAD2^{D166A}, DAD2^{N242I}, and DAD2$^{S96A/N242I}$) in the presence and absence of GR24, using differential scanning fluorimetry (DSF) assays. DAD2$^{F135A/N242I}$ was not included as it was not possible to express stable soluble protein. Consistent with our previous results (10, 30), DAD2^{WT} was observed to show a shift (ΔT_m) of −8.9 °C in its melting temperature, from 57.2 °C in the absence of GR24 to 48.3 °C in the presence of GR24 (Table 1 and Fig. S4). Compared with DAD2^{WT}, the DAD2 mutants, DAD2^{F135A}, DAD2^{D166A}, and DAD2^{N242I}, had lower melting temperatures in both the presence and absence of GR24 (Fig. S4 and Table 1). The overall ΔT_m for these mutants was observed to be greater than for DAD2^{WT} (−16.7 °C for DAD2^{F135A}, −13.0 °C for DAD2^{D166A}, and −13.6 °C for DAD2^{N242I}; Table 1). The DAD2$^{S96A/N242I}$ mutant also had a lower T_m in the absence of GR24; however, no changes were observed in the melting temperature of DAD2$^{S96A/N242I}$ in the presence of GR24 (Fig. S4 and Table 1), implying that this double mutant does not interact with GR24. Taken together, our results indicate that the DAD2^{F135A}, DAD2^{D166A}, and DAD2^{N242I} mutants are thermally less stable than DAD2^{WT}.

DAD2^{N242I} and DAD2^{D166A} are catalytically similar to DAD2^{WT}

We examined whether the DAD2 mutants are catalytically distinct from DAD2^{WT}, using a SL analogue, yoshimulactone green (YLG) as the substrate (31). We have previously shown that DAD2^{WT} displays a two-step hydrolysis mechanism, similar to AtD14, OsD14, and RMS3, using YLG; therefore all kinetic analyses in this study were conducted using a 15-min

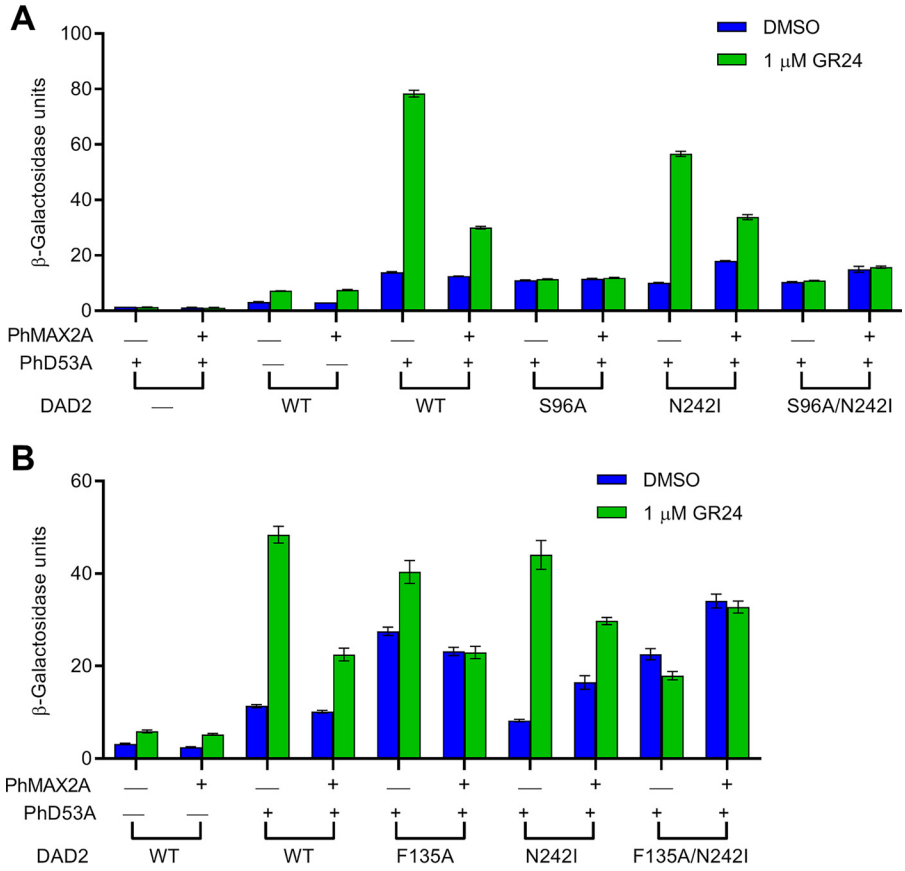

Figure 2. Interactions of DAD2 mutants with PhD53A in the presence and absence of PhMAX2A. *A* and *B* denote experiments conducted on separate occasions. Protein-protein interactions were quantified by assaying β-gal activity in the absence and presence of 1 μM GR24. WT DAD2 is indicated by WT. All data shown are mean ± S.E.; $n = 3$ technical replicates. Western blotting analyses confirming the presence of the fusion proteins in yeast are shown in Fig. S3.

Table 1

Melting temperatures of DAD2^{WT} and DAD2 mutants in the presence and absence of GR24

Protein	Melting temperature (T_m, °C)		Difference (ΔT_m, °C)
	DMSO	GR24	
DAD2^{WT}	57.2	48.3	−8.9
DAD2^{F135A}	53.0	36.3	−16.7
DAD2^{D166A}	56.0	43.0	−13.0
DAD2^{N242I}	51.2	37.6	−13.6
DAD2$^{S96A/N242I}$	48.2	48.5	+0.3

time point of the pre-steady-state phase (14, 29–31). Here, we refer to k_{cat} as the rate constant of the pre-steady-state phase and the $K_{½}$ as the YLG concentration that gives half the maximal velocity (V_{max} (14, 30)). DAD2^{N242I} and DAD2^{D166A} have similar kinetics to DAD2^{WT} (Fig. 3, *A* and *G*, and Table 2) and DAD2^{F135A} has a reduced k_{cat} (Table 2 and Fig. 3, *E* and *F*).

We have previously shown that the catalytic triad mutant of DAD2 (DAD2^{S96A}) is hydrolytically inactive when examined using TLC with GR24 as the substrate (10). Unexpectedly, weak hydrolytic activity toward the YLG substrate was detected in DAD2^{S96A} and DAD2$^{S96A/N242I}$ (Table 2 and Fig. 3, *C* and *D*). The observed weak YLG hydrolysis by DAD2^{S96A} was abolished when this mutant was subjected to heat denaturation (Fig. 3*C*). However, it should be noted that YLG is a nonnatural substrate (31). The observed weak hydrolysis of YLG by DAD2^{S96A} may therefore not be entirely relevant to SL hydrolysis by DAD2.

DAD2^{N242I} exhibits structural flexibility

To determine whether the N242I mutation has altered the conformation of DAD2, allowing it to interact with PhMAX2A in the absence of GR24, we solved the crystal structure of DAD2^{N242I} at 1.58 Å resolution, with two molecules of the mutant protein per asymmetric unit. Both molecules displayed the classical apo-SL receptor structure, with no major conformational change observed in either of the two protein molecules (Fig. 4 and Fig. S5). A MES molecule was bound within the catalytic cavity of the two DAD2^{N242I} molecules, where MES interacts with the catalytic Ser-96 and His-246 residues through hydrogen bonds (Fig. S6). DSF results showed that there was no significant shift in the melting temperature of DAD2^{WT} and DAD2^{N242I} in the presence of MES (Fig. S7), suggesting that MES binds to DAD2 with low affinity. It is likely that MES was present within the internal cavity of the protein in the crystal structure, because of its high concentration (0.1 M) in the crystallization solution.

Detailed comparisons of the DAD2^{N242I} structure with the structure of DAD2^{WT} highlighted small differences particularly in two core loops of both molecules of DAD2^{N242I}. The first loop, referred to here as the activation loop (A loop), consists of residues Thr-214–Pro-221 and shapes the entrance to the catalytic cavity. The second loop (Leu-241–Pro-248), referred to here as the mutation loop (M loop) containing the mutated N242I residue, connects the β7 sheet

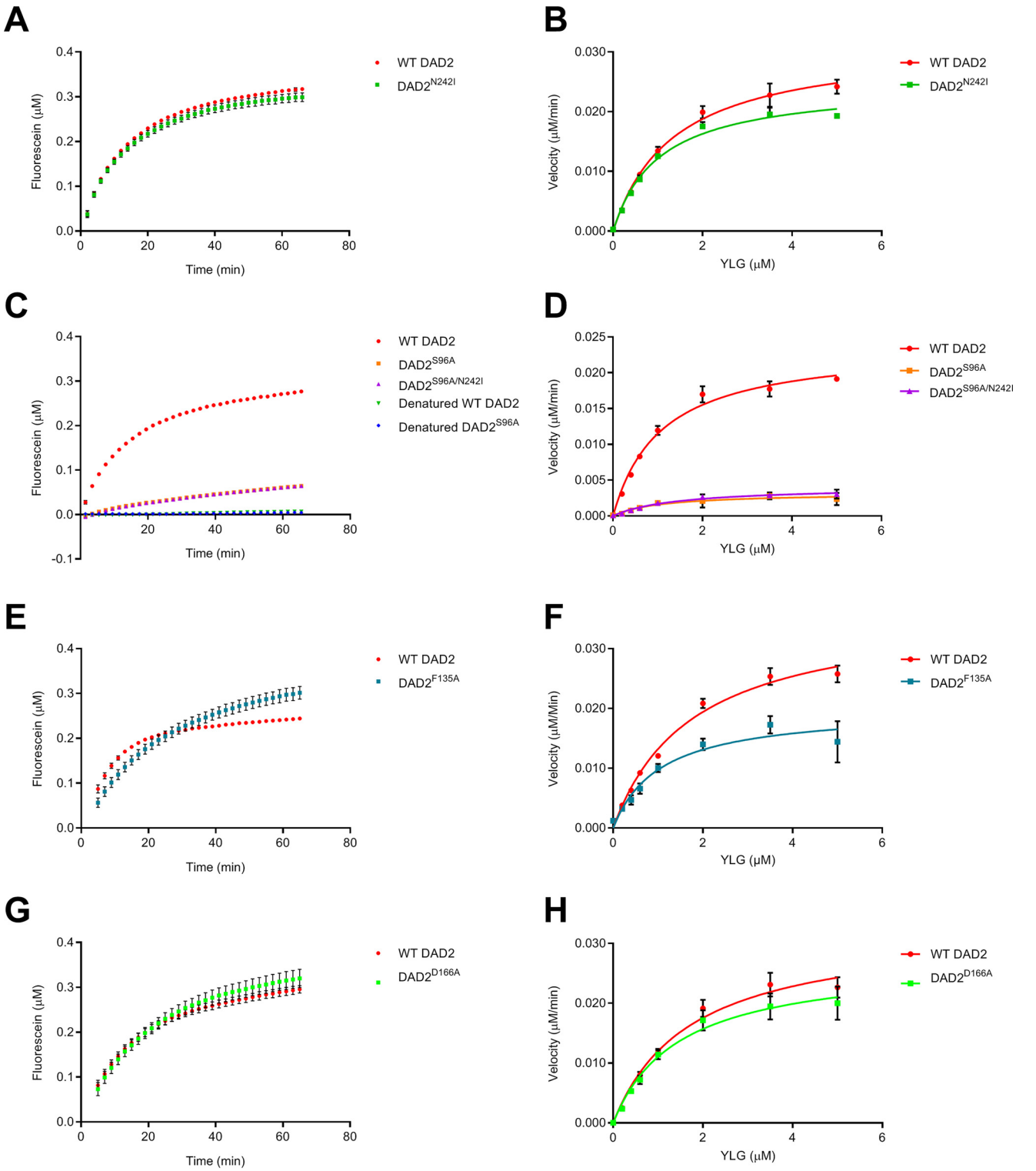

Figure 3. Hydrolysis of YLG by DAD2 mutants. *A*, *C*, *E*, and *G*, time course hydrolysis of 1 μM YLG by DAD2 mutants (0.34 μM protein) over 60 min. Denatured DAD2^{WT} (WT DAD2) and DAD2^{S96A} (S96A) were used as negative controls. *B*, *D*, *F*, and *H*, hydrolysis of YLG by DAD2 mutants (0.34 μM protein) at various YLG concentrations. Each data point is the mean ± S.E. of three technical replicates.

to the α11 helix (Fig. 4 and Fig. S5). In molecule A of the DAD2^{N242I} crystal structure, the A and M loops were displaced compared with those of DAD2^{WT}. In particular, a displacement of up to 2.5 Å was observed for the mutated residue at position 242 between DAD2^{WT} and DAD2^{N242I} (Fig. 4). Similar displacements, although of smaller amplitude, were also observed in molecule B of the asymmetric unit (Fig. S5). Apart from these two loops, other small displacements were also observed in the N-terminal end of the protein, the hairpin and the lid domain (αL1 and αL3 helices) of DAD2^{N242I} compared with DAD2^{WT} (Fig. 4 and Fig. S5).

Table 2
Kinetic parameters of DAD2^{WT} and DAD2 mutants

Protein	$K_{½}$	V_{max}	K_{cat}
	μM	$\mu M/min$	min^{-1}
DAD2^{WT}	1.36 ± 0.17	0.032	0.093 ± 0.004
DAD2^{S96A}	1.06 ± 0.57	0.003	0.010 ± 0.002
DAD2^{F135A}	1.05 ± 0.31	0.020	0.059 ± 0.006
DAD2^{D166A}	1.46 ± 0.33	0.027	0.080 ± 0.007
DAD2^{N242I}	1.03 ± 0.11	0.025	0.073 ± 0.003
DAD2$^{S96A/N242I}$	1.44 ± 0.35	0.004	0.012 ± 0.001

The DAD2^{N242I} mutant is more dynamic than DAD2^{WT}

Based on the observed differences between DAD2^{N242I} and DAD2^{WT}, it was hypothesized that DAD2^{N242I} might possess increased structural flexibility compared with DAD2^{WT}. To test this hypothesis, molecular dynamics (MD) simulations were performed using both DAD2^{WT} and DAD2^{N242I}. Examination of MD trajectories revealed similar overall movements, except in a few regions, particularly the αL2 helix-loop-αL3 helix region in the lid domain and the N termini of the proteins (Fig. 5 and Movie S1). The residues of these regions showed larger deviations from their initial positions in the DAD2^{N242I} structures than in DAD2^{WT} structures (Fig. 5). The root-mean-square fluctuation (RMSF), which quantifies the average deviation of the atomic positions of the residues from their average position during a simulation, also indicated that the residues comprising the αL2 helix-loop-αL3 helix region of the lid domain and the N terminus of DAD2^{N242I} have higher fluctuations than those of DAD2^{WT} (Fig. S8). By contrast, the residues comprising the A and M loops showed no significant differences in RMSF between the two models (Fig. 5 and Fig. S8).

A cluster analysis (in which the different structures that occur during the simulation were grouped based on their similarity as quantified by their RMSD (32, 33)) indicated that DAD2^{N242I} displays more flexibility than DAD2^{WT}, based on the observed number of clusters, the size of clusters, and the duration for which the clusters were present in the simulation (Fig. 6). For DAD2^{WT}, the most populated cluster, cluster 1, was populated for 84% of the simulation (~420 ns), and was continuously occupied for extended periods of time (Fig. 6*A*). The other clusters were only present transiently. By contrast, DAD2^{N242I} adopted several metastable conformations during the simulation, which was revealed by the appearance of several relatively short-lived clusters throughout the simulation (Fig. 6*B*). Furthermore, the most stable conformation adopted by DAD2^{N242I}, cluster 1, was present only for ~230 ns (*i.e.* 46%) of the total simulation. Taken together, the results from the MD simulations suggest that DAD2^{N242I} is more flexible than DAD2^{WT} and exhibits more dynamic states than DAD2^{WT}.

The D166A mutation does not affect the overall conformation of the protein

As described previously, the DAD2^{D166A} mutant retains its hydrolytic activity and interaction with PhD53A, but loses the ability to interact with PhMAX2A. To investigate the structural changes that could be responsible for this observation, we solved the crystal structure of DAD2^{D166A} at 1.52 Å resolution, with two molecules of the mutant protein in the asymmetric unit. Both DAD2^{D166A} molecules displayed a WT-like structure (10), with no structural changes (Fig. S9). Detailed comparison of the DAD2^{D166A} structure with that of DAD2^{WT} (PDB ID 4DNP (10)) showed only minor differences between the two proteins, specifically in the αL1 helix, αL3 helix, and the loop containing the mutated Ala-166 residue (referred to here as the D loop) of DAD2^{D166A} (Fig. S9).

To gain an understanding of the possible role of the D166A mutation, we examined the corresponding residue (Asp-167) in the orthologous protein AtD14 both in the unbound (open) state (12) and in the F-box-bound (closed) state (16). In the open state, the Asp-167 residue is located within the loop that connects the αL2 helix and αL3 helix of the lid domain, whereas in the closed state, this residue becomes part of the newly formed extended coil (Fig. S10). Moreover, the Asp-167 residue changes from being completely exposed in the open state, to being completely buried in the closed state. In the closed state, the side chain of Asp-167 forms two hydrogen bonds with the main chain atoms of the following valine residue (Val-168). Although Asp-167 is located within the interaction surface where the F-box protein has been reported to bind to the receptor (16), the buried side chain of this residue does not form a direct interaction with the F-box protein. This information suggests that disruption of electrostatic interactions with adjacent residues may be responsible for the effects of the DAD2^{D166A} mutation.

Discussion

In this work we aimed to address how the SL receptor gains the ability to interact with signaling partners during SL signal reception and transduction. We identified three mutants (DAD2^{N242I}, DAD2^{D166A}, and DAD2^{F135A}) in which we altered the ability of the receptor to interact with PhMAX2A and/or PhD53A in the presence or absence of SL. These mutants generally altered the interaction with one signaling partner, whereas not altering interaction with the other (Fig. S11), indicating that the SCF complex and PhD53A protein bind the receptor using different interaction surfaces and may affect the conformation of the receptor in different ways.

The N242I mutation enabled the protein to bypass the requirement for a ligand in the interaction with PhMAX2A but not with PhD53A, which was still dependent on SL (Fig. 1). The crystal structure of DAD2^{N242I} showed displacements of two loops compared with DAD2^{WT} (Fig. 4 and Fig. S5). The displacements near the site of the mutation (M and A loops) were thought to be due to direct effects of the mutation. In MD simulations, we observed that DAD2^{N242I} was more dynamic than DAD2^{WT}, with more short-lived transient conformations than DAD2^{WT}, which displayed a single conformation for most of the simulation (Fig. 6). The most dynamic region of the mutant protein was found to be the αL2 helix-loop-αL3 helix region of the lid domain (Movie S1 and Fig. S1). This region of the lid domain is in close proximity to the M loop, where the shift of the M loop may allow this region to become more flexible, resulting in the observed movement in the MD simulation.

In the AtD14-D3-ASK1 complex reported by Yao *et al.* (16) the αL2 helix-loop-αL3 helix region of the AtD14 receptor is part of the interaction surface and residues from this region such as Ala-160–Val-164, Glu-174, and Arg-177 are involved in

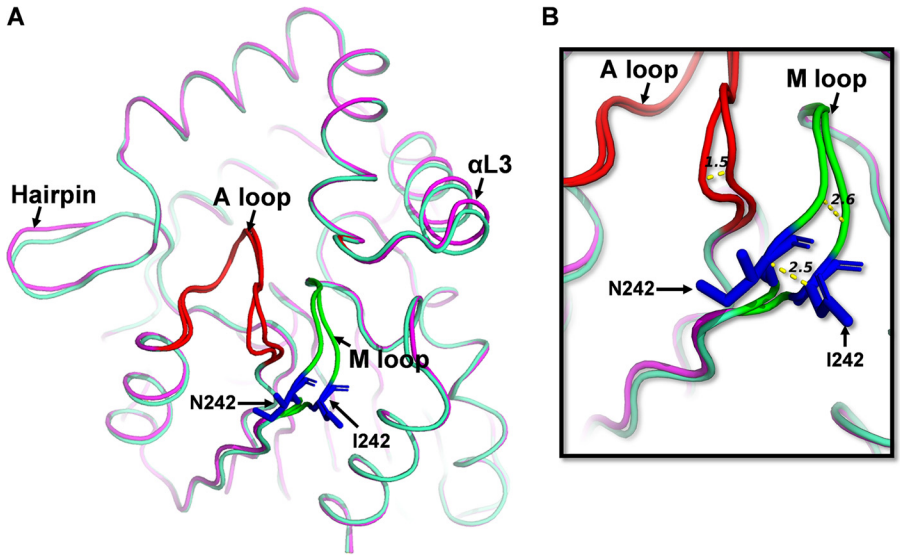

Figure 4. Structural comparison of DAD2^{WT} and molecule A of DAD2^{N242I}. *A,* structure of molecule A of DAD2^{N242I} protein (*light green*) superimposed onto the structure of DAD2^{WT} (*magenta*, PDB ID 4DNP) (10). The Asn-242 and Ile-242 residues are shown in stick representation in *blue*, the A loop in *red*, and the M loop in *fluorescent green*. *B,* the displacement of A and M loops (in Å, shown as *yellow dotted lines*) of molecule A of DAD2^{N242I} compared with that of DAD2^{WT}. Comparison of molecule B of DAD2^{N242I} and DAD2^{WT} is shown in Fig. S5. The DAD2^{N242I} protein also included a C89Q mutation to facilitate crystallization.

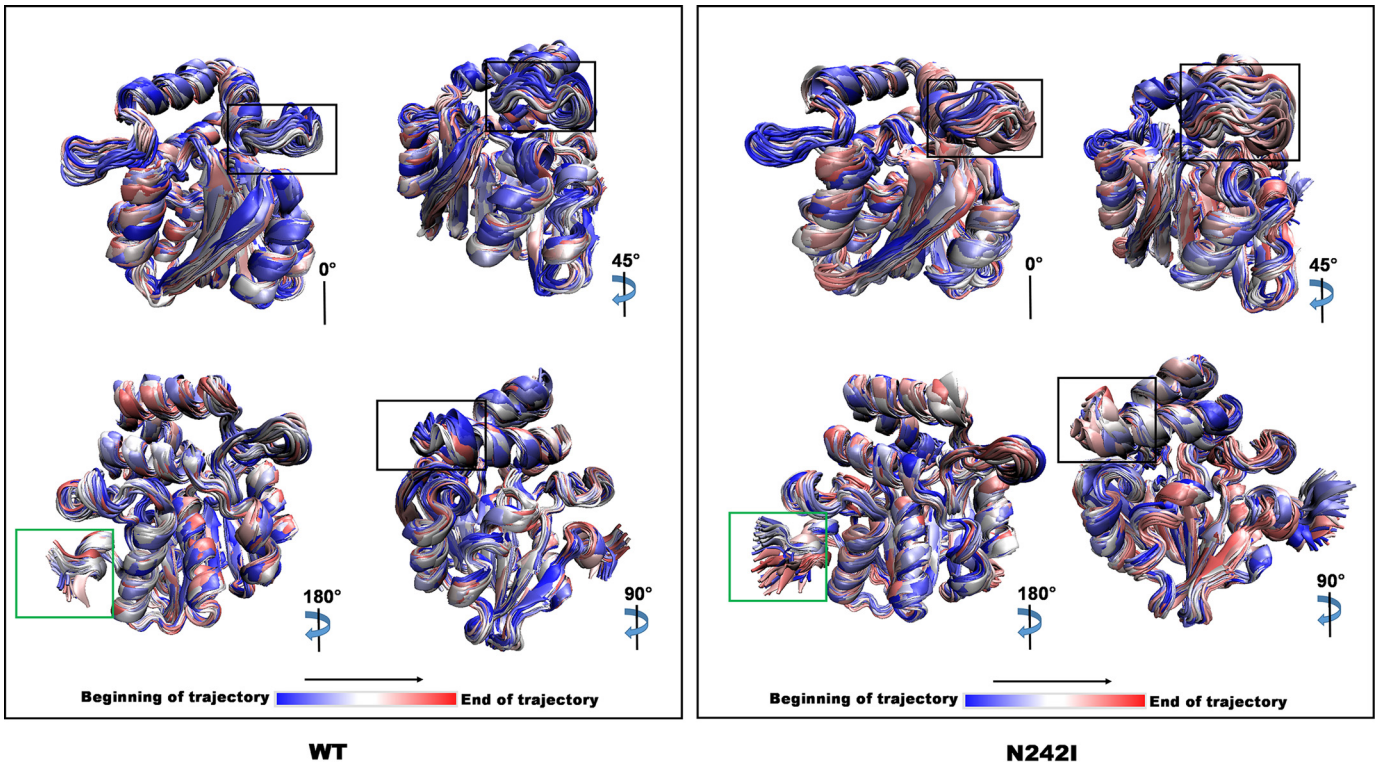

Figure 5. Visualization of DAD2^{WT} and DAD2^{N242I} MD simulation trajectories. Subset (first, every 100th and last) of structures present within the DAD2^{WT} (WT, *left*) and DAD2^{N242I} (N242I, *right*) MD simulation trajectories. The colors represent the start (*blue*), middle (*white*), and the end (*red*) of the simulation. The degree of rotation specified for each figure of WT or N242I is with respect to the structure shown in the *top left corner*. The αL2 helix-loop-αL3 helix region of the lid domain (highlighted in the *black box*) and the N terminus of the protein (highlighted in the *green box*) show the most differences in movement between the WT and N242I simulations.

the interaction with the F-box D3 protein. Based on these observations and the movements of this region of the DAD2^{N242I} model, we propose that it is the increased flexibility of the αL2 helix-loop-αL3 helix region that allows DAD2^{N242I} to interact with PhMAX2A. We predict that the movement of this region exposes key residues, perhaps transiently, including residues that are buried under the αL3 lid helix, and makes them available for interaction with PhMAX2A. The flexibility of this region could also facilitate the conformational changes required for the interaction between the DAD2^{N242I} mutant and PhMAX2A protein.

It is possible that the N242I mutation does not affect the flexibility of regions of the mutant protein involved in, or required for, binding of the PhD53A protein, which is fulfilled

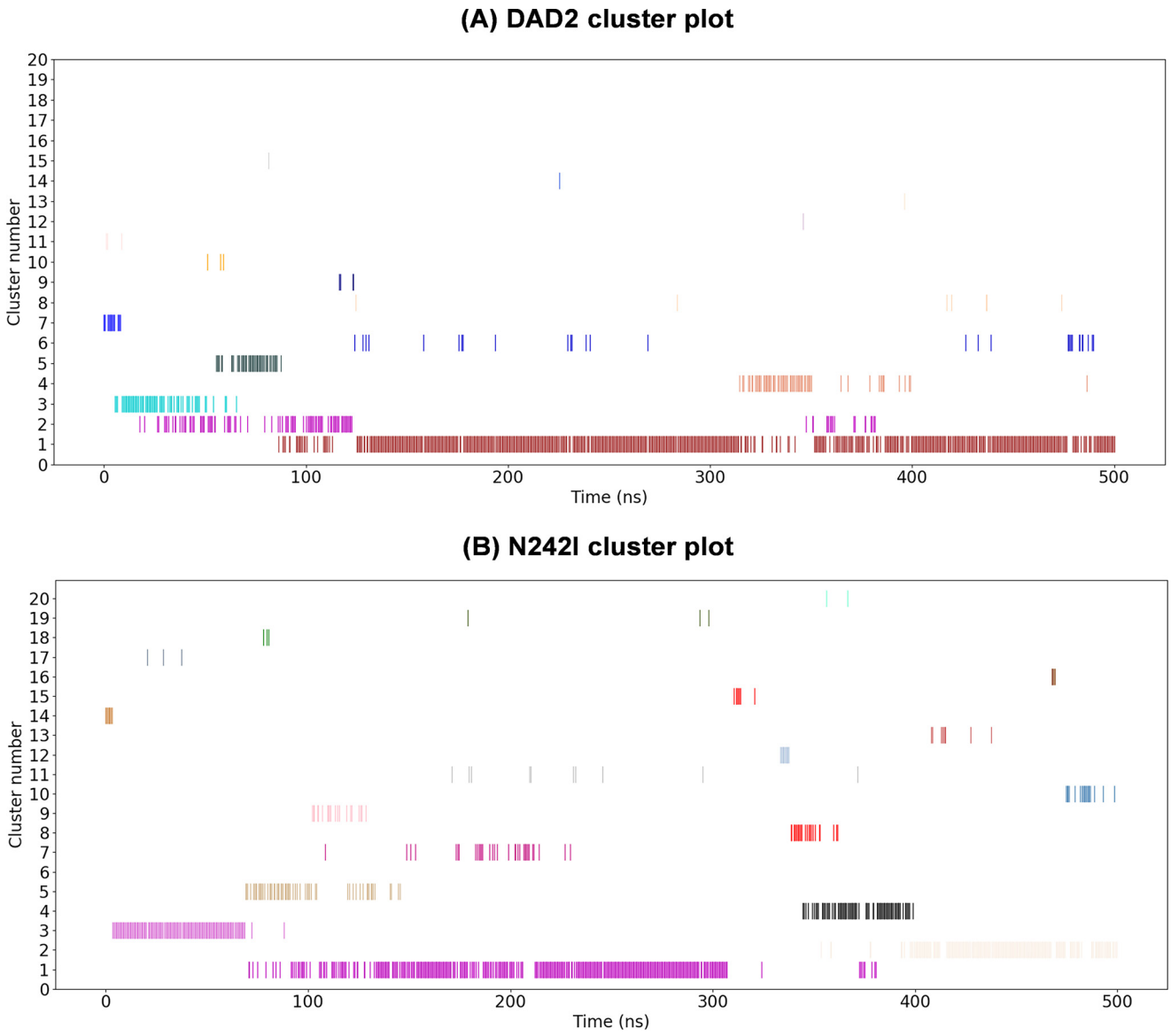

Figure 6. Cluster analysis of DAD2^{WT} and DAD2^{N242I} MD simulations. Cluster time series plots of DAD2^{WT} (*A*) and DAD2^{N242I} (*B*) showing cluster occupation *versus* the simulation time (in ns). Each cluster is represented as a *horizontal series of lines* in a specific color where each line represents occupancy of that cluster at that point in time. Clusters are ordered from the most (*1*) to the least (*20*) populated. The cluster analysis highlights that DAD2^{N242I} is more dynamic as it occupies several clusters throughout the simulation, whereas DAD2^{WT} mostly exists in a single stable conformation represented by cluster 1. The cluster program identified 15 clusters for DAD2^{WT} and 26 clusters for DAD2^{N242I} at the specified cut-off of 0.15 nm. The DAD2^{WT} plot depicts all of the identified 15 clusters, whereas the DAD2^{N242I} plot depicts the most populated 20 clusters from the identified 26 clusters.

by the presence of SL. Indeed the DAD2$^{S96A/N242I}$ mutant, which has severely reduced hydrolytic activity, is unable to interact with PhD53A in the presence of SL. However, it can still interact with PhMAX2A with or without SL, suggesting that SL alters the flexibility of different regions of the receptor protein to enable interaction with signaling partners. This is consistent with the altered T_m observed for the mutant receptor in the absence of SL and is consistent with the observations of Zhao *et al.* (19). The SL-independent interaction detected between DAD2^{N242I} and PhD53A in the presence of PhMAX2A in yeast two-hybrid experiments (Fig. 2*B*) also suggests that the binding of the F-box protein enables the mutant receptor to undergo further conformational change(s) that favors the recruitment of the target protein, PhD53A, to the SCF complex.

Similar to DAD2^{N242I}, the DAD2^{F135A} mutant has hormone-independent interactions, in this case with PhD53A, whereas its interaction with PhMAX2A is still dependent on SL (Fig. 1). In the absence of SL, the interaction with PhD53A remained unaffected by the presence or absence of PhMAX2A (Fig. 2). However, in combination with the N242I mutation, we observed an increase in hormone-independent interaction between the double mutant (DAD2$^{F135A/N242I}$) and PhD53A in the presence of PhMAX2A (Fig. 2), suggesting that the double mutant is forming a ternary complex with both proteins. In the DSF assays, DAD2^{F135A} showed a lower T_m than DAD2^{WT} (Table 1 and Fig. S4). It is possible that, like the DAD2^{N242I} mutant, both DAD2^{F135A} and DAD2$^{F135A/N242I}$ have increased flexibility in specific regions of the receptor that enable these mutants to interact, respectively, with one or two of the downstream part-

ners (Fig. S11). However, we have not been able to solve the structures of these mutants and larger conformational changes remain a possibility for being responsible for their altered interactions with signaling partners, and altered kinetic properties in the case of $DAD2^{F135A}$.

The D166A mutation led to a loss of interaction with PhMAX2A in the presence of SL without affecting interaction with PhD53A (Fig. 1). Like $DAD2^{N242I}$, this mutant has WT-like hydrolytic activity, was found to be thermally less stable than the WT receptor, and there were no obvious conformational changes in the $DAD2^{D166A}$ crystal structure (Fig. 3, Tables 1 and 2, and Figs. S4 and S9). The Asp-166 residue is situated in the loop that connects the αL2 lid helix to the αL3 lid helix and is conserved in most identified SL receptor orthologs, but is not directly involved in the interaction with the F-box protein. Instead it is likely that replacement of Asp-166 with an Ala residue has its effect by preventing key electrostatic interactions required for the receptor to adopt the closed state in which it interacts with the F-box protein.

Our work using MD simulations suggests the hypothesis that flexibility of certain regions of the receptor can affect the ability to interact with signaling partners, although we consider it unlikely that we have fully identified all regions involved (Fig. S11). With respect to the SCF complex, Zhao *et al.* (19) and Yao *et al.* (16) have identified regions of the SL receptor that are involved in the interaction with the F-box protein. These regions include the helices of the lid and the loop that shapes the entrance of the cavity (referred to here as the A loop). In the crystal structure of the AtD14-D3-ASK1 complex by Yao *et al.* (16), the A loop becomes disordered, whereas the lid helices undergo changes and move toward each other to close the entrance of the cavity to create the interaction surface. In our previous work, we also showed that a residue of the A loop interacts with a SL receptor antagonist, tolfenamic acid, effectively locking the receptor in the open form (30). The flexibility of this loop may therefore also be involved in the ability of the receptor to interact with signaling partners.

In this and other work (19, 28), it is evident that SL signaling can be activated in the absence of the ligand or hydrolytic activity of the receptor. However, phylogenetic comparisons show the catalytic triad is conserved in all SL receptors examined (34). It is possible that hydrolysis may still be involved in removing SL from the cell after it is perceived, although it is currently unknown if other proteins can also fulfil this role or if hydrolysis and/or the catalytic triad is required for another function. Furthermore, the hydrolytic products of the receptor do not have biological activity, at least with respect to altering branching in plants (10, 15, 35, 36), however, it remains possible that these products may still have a role that is currently unknown.

Perception of SL appears to be a surprisingly complex process (26). The data presented here demonstrate that it is possible to bypass the need for ligand hydrolysis by introducing mutations that have an effect on the flexibility of specific regions of the SL receptor that are involved in interactions with downstream signaling partners. This is consistent with the findings of Seto *et al.* (28) and Zhao *et al.* (19). Such a hydrolysis-independent mechanism may also be regulated by the SCF complex as suggested by Shabek *et al.* (29). A major goal to shed further light on the changes occurring in the receptor upon binding of its partners is to solve the structure of a complex containing the receptor as well as the F-box protein and a target (*e.g.* the repressor protein D53) of the receptor-SCF complex.

Experimental procedures

Mutagenesis of DAD2

Amino acid mutations were introduced into the bacterial codon-optimized ORF of DAD2. Random mutagenesis was performed using an error-prone PCR polymerase using the GeneMorph® II Random EZClone Domain Mutagenesis kit according to the manufacturer's instructions (Agilent Technologies). Site-directed mutagenesis was performed using the QuikChange® Lightning Site-directed Mutagenesis kit (Agilent Technologies) according to the manufacturer's instructions.

A C89Q mutation was introduced into the $DAD2^{D166A}$, $DAD2^{F135A}$, and $DAD2^{N242I}$ constructs to obtain protein crystals with good diffraction (30). $DAD2^{D166A}$ used in the DSF and YLG hydrolysis assays also contained the C89Q mutation. The C89Q mutation in DAD2 does not alter the function of the proteins in terms of SL hydrolysis (see Fig. S12) and SL binding (30).

Expression and purification of recombinant proteins

DAD2 and its mutants were expressed as fusion proteins with a cleavable, N-terminal His_6-MBP tag in *Escherichia coli* Rosetta gami-2 (DE3) cells (Novagen, USA) overnight at 20 °C. The cells were harvested and homogenized twice using an EmusiFlex C3 (Avestin) at 10,000–15,000 p.s.i. The soluble fraction was purified by metal affinity chromatography using a 5-ml HisTrap™ HP column (GE Healthcare) and eluted with 20 mM Tris-HCl (pH 8.0), 100 mM NaCl, 300 mM imidazole. The eluted protein was dialyzed against 20 mM Tris-HCl (pH 8.0), 50 mM NaCl, and 1 mM DTT (for proteins used for crystallization, dialysis was performed in the same buffer without DTT) at 4 °C for 16 h and further purified by anion-exchange using a 5-ml HiTrap™ Q HP column (GE healthcare). Proteins were eluted using a continuous salt gradient of 0–500 mM in 20 mM Tris-HCl (pH 8.0) and 1 mM DTT (proteins used for crystallization were eluted in the same condition without DTT). The His_6-MBP tag was then cleaved using tobacco etch virus protease at a protease:protein ratio of 1:50 (w/w) at 4 °C by dialyzing against 20 mM Tris-HCl (pH 8), 150 mM NaCl, 50 mM L-arginine, 50 mM L-glutamic acid, 1 mM DTT, and 1 mM EDTA. The cleaved protein was then dialyzed against the same buffer lacking 1 mM DTT and 1 mM EDTA for 2 h at 4 °C before being subjected to another round of metal affinity chromatography. The flow-through containing purified protein was collected, concentrated to ~6 mg/ml, and stored at −80 °C. For the $DAD2^{D166A}$ mutant, anion-exchange chromatography was not performed. Prior to crystallization, YLG hydrolysis, and DSF assays, the proteins were buffer-exchanged into 20 mM Tris-HCl (pH 8.0) and 150 mM NaCl (proteins used for YLG hydrolysis and DSF assays were exchanged into buffer containing 1 mM DTT) using Superdex™ 75 100/300 GL column (GE Healthcare) and concentrated, if required for an experiment.

Crystallization

The crystallization experiments were performed by a hanging drop vapor diffusion method at room temperature. For $DAD2^{N242I}$, the initial crystal hits were obtained in two conditions, the first comprising 0.1 M MES (pH 6.5) and 1.6 M magnesium sulfate, and the second comprising 0.1 M sodium cacodylate (pH 6.5) and 1.4 M sodium acetate. Crystals used for data collection were obtained in a condition containing 0.9 μl of 7 mg/ml of $DAD2^{N242I}$ in the presence of 0.1 M MES buffer (pH 6.5) with 1.58 M $MgSO_4$ or 1.72 M $MgSO_4$. For $DAD2^{D166A}$, initial crystal hits were obtained in several conditions of the Morpheus screen (Molecular Dimension Ltd.). The condition containing 0.1 M Trizma-Bicine (pH 8.5), 30 mM $MgCl_2$, 30 mM $CaCl_2$, and 20% (v/v) PEG 500 monomethyl ether, 10% (v/v) PEG 20000 was further refined and crystals used for data collection were obtained in conditions containing 0.9 μl of 5 mg/ml of $DAD2^{D166A}$ in the presence of 0.1 M Trizma-acetate-Bicine (pH 8.5), 30 mM $MgCl_2$, 30 mM $CaCl_2$, and 18–22% PEG 500 monomethyl ether, 9–11% PEG 20000. The crystals used for data collection were obtained in a condition comprised of 0.1 M Trizma-acetate-Bicine (pH 8.5), 30 mM $MgCl_2$, 30 mM $CaCl_2$, and 20% (v/v) PEG 500 monomethyl ether, 10% PEG 20000. A small amount of $DAD2^{F135A}$ was obtained and crystallized in 0.1 M Trizma-acetate-Bicine (pH 8.5), 30 mM $MgCl_2$, 30 mM $CaCl_2$, and 12% (v/v) PEG 500 monomethyl ether, 6% PEG 20000.

Data collection, processing, and structure determination

Complete datasets were collected at the Australian synchrotron (Victoria, Australia). The dataset for the $DAD2^{N242I}$ protein crystal was collected on the MX2 beamline to a resolution of 1.58 Å. The dataset for the $DAD2^{D166A}$ crystals was collected on the MX1 beamline to a resolution of 1.52 Å. Data indexing and integration were performed using iMOSFLM or XDS (37, 38). The intensities were merged using aimless/pointless from the CCP4 suite (39–41). The number of molecules in the asymmetric unit were determined using Matthew's coefficient from the CCP4 suite. Structures were solved by molecular replacement using the crystal structure of WT DAD2 ($DAD2^{WT}$; PDB ID 4DNP) as the model in PHASER MR from CCP4 suite (42, 43). Structure refinement and subsequent cycles of model building were performed in REFMAC5 and COOT, respectively (44, 45). The final models were refined using the optimized parameters obtained from the PDB redo server. The statistics for data collection and refinement are listed in Table S1. Crystals obtained with $DAD2^{F135A}$ showed only poor diffraction and were not analyzed further.

MD simulations

The initial coordinates for the $DAD2^{WT}$ and $DAD2^{N242I}$ models were obtained from their respective crystal structures (DAD2, PDB ID 4DNP, and $DAD2^{N242I}$, PDB ID 6UH8, molecule A of the asymmetric unit). The crystallographic water and any ligands were removed from the PDB file. The simulations were performed using the Gromacs software, version 2016.1 (SCR_014545 (46)) and the Amber force field, FF99SB (47). Periodic boundary conditions were used with a cubic simulation box with sides of 2 nm from the solute in all directions. The systems were solvated using the TIP3P (48) water model. All amino acids were assumed to be in their standard protonation state at physiological pH (~7), resulting in a net charge of −4 for $DAD2^{WT}$ and −5 for $DAD2^{N242I}$. Sodium ions were added to ensure an overall net neutral system. All simulations were performed using a 2-fs integration time step with the covalent bond lengths involving hydrogen atoms constrained using LINCS (49). Nonbonded interactions were calculated explicitly up to a cut-off of 1.2 nm. Outside this, long-range electrostatic interactions were calculated using Particle Mesh Ewald summation (50). The temperature was maintained using the Velocity Rescale Thermostat (51) and for the NPT simulations, constant pressure was maintained using the Berendsen barostat (52). The systems underwent a two-stage energy minimization comprising 5000 steps using the steepest descent algorithm followed by 5000 steps with the conjugate gradient algorithm. The systems were then heated from 50 to 298 K over 250 ps at a heating rate of 1 K/ps in the NVT ensemble, followed by a short (250 ps) equilibration simulation under NPT conditions (298 K, 1 atm). Production simulations were then performed in the NPT ensemble for 500 ns at 298 K and 1 atm pressure.

Analysis of MD simulation data

The MD simulation data were analyzed using Gromacs (version 2016.1; SCR_014545 (46)) tools and visualized using Visual Molecular Dynamics (VMD) (version 1.9.3; SCR_001820 (53)). For cluster analysis, only every 100th frame was considered to make the all-by-all RMSD calculations required for cluster analysis tractable. Clustering was performed using the Gromaos algorithm and a root-mean-square deviation (RMSD) cut-off of 0.15 nm. This cut-off value was selected as it gave a manageable number of clusters (*i.e.* less than 50). Occupation of the most populated 20 clusters was then plotted against the time series of the simulation using an in-house Python script. For RMSF analysis, the main trajectory files of the two models were used and the analysis was performed using the RMSF tool of Gromacs.

Differential scanning fluorimetry

DSF experiments were performed as described in Hamiaux *et al.* (10). Reaction mixtures were set up in 384 multiwell plates at a molar ratio of 25:1 (GR24:protein). Each reaction, in a final volume of 20 μl, consisted of 250 μM (*rac*)-GR24, 10 μM protein, and ×10 Sypro™ Tangerine protein dye in 20 μM Tris-HCl (pH 8.0), 150 mM NaCl, and 2.5% DMSO. The final reaction mixture for the DMSO control consisted of the same assay components without (*rac*)-GR24.

DSF assays were also performed using MES as a test compound. Various concentrations of MES were tested (0.25–128 mM). The experiment was setup in a similar method as described above with MES instead of (*rac*)-GR24.

YLG hydrolysis assays

The hydrolytic activity of DAD2 mutants was determined using YLG (TCI Chemicals) according to the methods of Tsuchiya *et al.* (31) with some modifications. To determine the time course hydrolysis of YLG, each reaction mixture (in a final volume of 100 μl) consisted of 0.34 μM protein and 1 μM YLG in

20 mM Tris-HCl (pH 8.0), 150 mM NaCl, and 1% DMSO. The YLG control consisted of 1 μM YLG in the same buffer. For kinetics analyses, assay reactions were performed at seven YLG concentrations (0, 0.2, 0.4, 0.6, 1.2, 3.5, and 5 μM) in triplicate. Protein concentration and reaction buffer were the same as the time course hydrolysis assays. All experiments were conducted in three technical replicates. Fluorescence was monitored using a FLUOStar® Omega microplate reader (BMG LabTech) with 485 $\pm$ 12 nm excitation filter and 520 $\pm$ 10 nm emission filter every 2 min over a 60-min interval. The gain was set to 920, and the number of flashes to 20. Fluorescence units were converted to fluorescein concentrations using fluorescein standard curves. Velocity (μM/min) at each YLG concentration was calculated as the amount of fluorescein produced (μM) per minute. Michaelis-Menten analyses were determined by nonlinear regression in GraphPad Prism using the velocity at the 15-min time point.

Yeast two-hybrid assays

Yeast two-hybrid experiments were performed by β-gal liquid culture assay according to methods from the Clontech Yeast Protocols Handbook (2009). DAD2^{WT} and DAD2 mutants were cloned into a pBD vector, whereas PhMAX2A and PhD53A were cloned into a pAD vector for expression in yeast PJ69-4 (54, 55). The pURA3-GW vector was used to express PhMAX2A as a third untagged protein when required in the yeast assays. Yeast transformants were subjected to Western blot analysis to confirm the presence of the binding domain and activation domain fusion proteins (30). The strength of DAD2-PhMAX2A and DAD2-PhD53A interactions compared with DMSO controls were quantified using orthonitro-phenyl-β-galactopyranoside (Sigma-Aldrich) as the substrate in the presence of 10 and 1 μM (*rac*)-GR24, respectively.

Accession numbers

The crystal structure of DAD2^{N242I} has been deposited in the Protein Data Bank under PDB ID 6UH8, and the crystal structure of DAD2^{D166A} under PDB ID 6UH9.

Author contributions—H. W. L., P. S., C. H., and K. C. S. data curation; H. W. L., P. S., B. J. J., R. S. D., Z. L., C. H., T. C., J. R. A., and K. C. S. formal analysis; H. W. L., P. S., B. J. J., R. S. D., Z. L., and T. C. investigation; H. W. L., P. S., and K. C. S. visualization; H. W. L., P. S., B. J. J., R. S. D., C. H., and J. R. A. methodology; H. W. L., P. S., and K. C. S. writing-original draft; B. J. J. and K. C. S. conceptualization; B. J. J. and K. C. S. funding acquisition; B. J. J., C. H., J. R. A., and K. C. S. writing-review and editing; R. S. D. validation; C. H., T. C., J. R. A., R. D. N., and K. C. S. supervision; K. C. S. project administration.

Acknowledgments—We thank members of the Laboratory of Structural Biology (University of Auckland) for help with X-ray data collection, and Colm Carraher and Donald Hunter for comments on the manuscript. Crystallography data were collected on the MX1 and MX2 beamlines at the Australian Synchrotron, part of ANSTO (Victoria, Australia).

References

1. Cook, C. E., Whichard, L. P., Turner, B., Wall, M. E., and Egley, G. H. (1966) Germination of witchweed (*Striga lutea* Lour.): isolation and properties of a potent stimulant. *Science* **154,** 1189–1190 CrossRef Medline
2. Yokota, T., Sakai, H., Okuno, K., Yoneyama, K., and Takeuchi, Y. (1998) Alectrol and orobanchol, germination stimulants for *Orobanche minor*, from its host red clover. *Phytochemistry* **49,** 1967–1973 CrossRef
3. Akiyama, K., Matsuzaki, K., and Hayashi, H. (2005) Plant sesquiterpenes induce hyphal branching in arbuscular mycorrhizal fungi. *Nature* **435,** 824–827 CrossRef Medline
4. Gomez-Roldan, V., Fermas, S., Brewer, P. B., Puech-Pagès, V., Dun, E. A., Pillot, J. P., Letisse, F., Matusova, R., Danoun, S., Portais, J. C., Bouwmeester, H., Becard, G., Beveridge, C. A., Rameau, C., and Rochange, S. F. (2008) Strigolactone inhibition of shoot branching. *Nature* **455,** 189–194 CrossRef Medline
5. Umehara, M., Hanada, A., Yoshida, S., Akiyama, K., Arite, T., Takeda-Kamiya, N., Magome, H., Kamiya, Y., Shirasu, K., Yoneyama, K., Kyozuka, J., and Yamaguchi, S. (2008) Inhibition of shoot branching by new terpenoid plant hormones. *Nature* **455,** 195–200 CrossRef Medline
6. Kapulnik, Y., Delaux, P.-M., Resnick, N., Mayzlish-Gati, E., Wininger, S., Bhattacharya, C., Séjalon-Delmas, N., Combier, J.-P., Bécard, G., Belausov, E., Beeckman, T., Dor, E., Hershenhorn, J., and Koltai, H. (2011) Strigolactones affect lateral root formation and root-hair elongation in *Arabidopsis*. *Planta* **233,** 209–216 CrossRef Medline
7. Ruyter-Spira, C., Kohlen, W., Charnikhova, T., van Zeijl, A., van Bezouwen, L., de Ruijter, N., Cardoso, C., Lopez-Raez, J. A., Matusova, R., Bours, R., Verstappen, F., and Bouwmeester, H. (2011) Physiological effects of the synthetic strigolactone analog GR24 on root system architecture in *Arabidopsis*: another belowground role for strigolactones? *Plant Physiol.* **155,** 721–734 CrossRef Medline
8. Snowden, K. C., Simkin, A. J., Janssen, B. J., Templeton, K. R., Loucas, H. M., Simons, J. L., Karunairetnam, S., Gleave, A. P., Clark, D. G., and Klee, H. J. (2005) The decreased apical dominance1/Petunia hybrida CAROTENOID CLEAVAGE DIOXYGENASE8 gene affects branch production and plays a role in leaf senescence, root growth, and flower development. *Plant Cell* **17,** 746–759 CrossRef Medline
9. Yamada, Y., Furusawa, S., Nagasaka, S., Shimomura, K., Yamaguchi, S., and Umehara, M. (2014) Strigolactone signaling regulates rice leaf senescence in response to a phosphate deficiency. *Planta* **240,** 399–408 CrossRef Medline
10. Hamiaux, C., Drummond, R. S., Janssen, B. J., Ledger, S. E., Cooney, J. M., Newcomb, R. D., and Snowden, K. C. (2012) DAD2 Is an α/β hydrolase likely to be involved in the perception of the plant branching hormone, strigolactone. *Curr. Biol.* **22,** 2032–2036 CrossRef Medline
11. Arite, T., Umehara, M., Ishikawa, S., Hanada, A., Maekawa, M., Yamaguchi, S., and Kyozuka, J. (2009) D14, a strigolactone-insensitive mutant of rice, shows an accelerated outgrowth of tillers. *Plant Cell Physiol.* **50,** 1416–1424 CrossRef Medline
12. Zhao, L. H., Zhou, X. E., Wu, Z. S., Yi, W., Xu, Y., Li, S., Xu, T. H., Liu, Y., Chen, R. Z., Kovach, A., Kang, Y., Hou, L., He, Y., Xie, C., Song, W., *et al.* (2013) Crystal structures of two phytohormone signal-transducing α/β hydrolases: karrikin-signaling KAI2 and strigolactone-signaling DWARF14. *Cell Res.* **23,** 436–439 CrossRef Medline
13. Chevalier, F., Nieminen, K., Sanchez-Ferrero, J. C., Rodríguez, M. L., Chagoyen, M., Hardtke, C. S., and Cubas, P. (2014) Strigolactone promotes degradation of DWARF14, an α/β hydrolase essential for strigolactone signaling in *Arabidopsis*. *Plant Cell* **26,** 1134–1150 CrossRef Medline
14. de Saint Germain, A., Clavé, G., Badet-Denisot, M.-A., Pillot, J.-P., Cornu, D., Le Caer, J.-P., Burger, M., Pelissier, F., Retailleau, P., Turnbull, C., Bonhomme, S., Chory, J., Rameau, C., and Boyer, F.-D. (2016) An histidine covalent receptor and butenolide complex mediates strigolactone perception. *Nat. Chem. Biol.* **12,** 787–794 CrossRef Medline
15. Nakamura, H., Xue, Y. L., Miyakawa, T., Hou, F., Qin, H. M., Fukui, K., Shi, X., Ito, E., Ito, S., Park, S. H., Miyauchi, Y., Asano, A., Totsuka, N., Ueda, T., Tanokura, M., and Asami, T. (2013) Molecular mechanism of strigolactone perception by DWARF14. *Nat. Commun.* **4,** 2613 CrossRef Medline

16. Yao, R., Ming, Z., Yan, L., Li, S., Wang, F., Ma, S., Yu, C., Yang, M., Chen, L., Chen, L., Li, Y., Yan, C., Miao, D., Sun, Z., Yan, J., *et al.* (2016) DWARF14 is a non-canonical hormone receptor for strigolactone. *Nature* **536,** 469–473 CrossRef Medline
17. Yao, R., Wang, L., Li, Y., Chen, L., Li, S., Du, X., Wang, B., Yan, J., Li, J., and Xie, D. (2018) Rice DWARF14 acts as an unconventional hormone receptor for strigolactone. *J. Exp. Botany* **69,** 2355–2365 CrossRef Medline
18. Waters, M. T., Scaffidi, A., Flematti, G., and Smith, S. M. (2015) Substrate-induced degradation of the α/β-fold hydrolase KARRIKIN INSENSITIVE2 requires a functional catalytic triad but is independent of MAX2. *Mol. Plant* **8,** 814–817 CrossRef Medline
19. Zhao, L.-H., Zhou, X. E., Yi, W., Wu, Z., Liu, Y., Kang, Y., Hou, L., de Waal, P. W., Li, S., Jiang, Y., Scaffidi, A., Flematti, G. R., Smith, S. M., Lam, V. Q., Griffin, P. R., *et al.* (2015) Destabilization of strigolactone receptor DWARF14 by binding of ligand and E3-ligase signaling effector DWARF3. *Cell Res.* **25,** 1219–1236 CrossRef Medline
20. Abe, S., Sado, A., Tanaka, K., Kisugi, T., Asami, K., Ota, S., Kim, H. I., Yoneyama, K., Xie, X., Ohnishi, T., Seto, Y., Yamaguchi, S., Akiyama, K., Yoneyama, K., and Nomura, T. (2014) Carlactone is converted to carlactonoic acid by MAX1 in *Arabidopsis* and its methyl ester can directly interact with AtD14 *in vitro*. *Proc. Natl. Acad. Sci. U.S.A.* **111,** 18084–18089 CrossRef Medline
21. Liang, Y., Ward, S., Li, P., Bennett, T., and Leyser, O. (2016) SMAX1-LIKE7 signals from the nucleus to regulate shoot development in *Arabidopsis* via partially EAR motif-independent mechanisms. *Plant Cell* **28,** 1581–1601 Medline
22. Jiang, L., Liu, X., Xiong, G., Liu, H., Chen, F., Wang, L., Meng, X., Liu, G., Yu, H., Yuan, Y., Yi, W., Zhao, L., Ma, H., He, Y., Wu, Z., *et al.* (2013) DWARF 53 acts as a repressor of strigolactone signalling in rice. *Nature* **504,** 401–405 CrossRef Medline
23. Zhou, F., Lin, Q., Zhu, L., Ren, Y., Zhou, K., Shabek, N., Wu, F., Mao, H., Dong, W., Gan, L., Ma, W., Gao, H., Chen, J., Yang, C., *et al.* (2013) D14-SCF(D3)-dependent degradation of D53 regulates strigolactone signalling. *Nature* **504,** 406–410 CrossRef Medline
24. Wang, L., Wang, B., Jiang, L., Liu, X., Li, X., Lu, Z., Meng, X., Wang, Y., Smith, S. M., and Li, J. (2015) Strigolactone signaling in *Arabidopsis* regulates shoot development by targeting D53-like SMXL repressor proteins for ubiquitination and degradation. *Plant Cell* **27,** 3128–3142 CrossRef Medline
25. Soundappan, I., Bennett, T., Morffy, N., Liang, Y., Stanga, J. P., Abbas, A., Leyser, O., and Nelson, D. C. (2015) SMAX1-LIKE/D53 family members enable distinct MAX2-dependent responses to strigolactones and karrikins in *Arabidopsis*. *Plant Cell* **27,** 3143–3159 Medline
26. Machin, D. C., Hamon-Josse, M., and Bennett, T. (2019) Fellowship of the rings: a saga of strigolactones and other small signals. *New Phytol.* **225,** 621–636 Medline
27. Kagiyama, M., Hirano, Y., Mori, T., Kim, S. Y., Kyozuka, J., Seto, Y., Yamaguchi, S., and Hakoshima, T. (2013) Structures of D14 and D14L in the strigolactone and karrikin signaling pathways. *Genes Cells* **18,** 147–160 CrossRef
28. Seto, Y., Yasui, R., Kameoka, H., Tamiru, M., Cao, M., Terauchi, R., Sakurada, A., Hirano, R., Kisugi, T., Hanada, A., Umehara, M., Seo, E., Akiyama, K., Burke, J., Takeda-Kamiya, N., *et al.* (2019) Strigolactone perception and deactivation by a hydrolase receptor DWARF14. *Nat. Commun.* **10,** 191 CrossRef Medline
29. Shabek, N., Ticchiarelli, F., Mao, H., Hinds, T. R., Leyser, O., and Zheng, N. (2018) Structural plasticity of D3–D14 ubiquitin ligase in strigolactone signalling. *Nature* **563,** 652–656 CrossRef Medline
30. Hamiaux, C., Drummond, R. S. M., Luo, Z., Lee, H. W., Sharma, P., Janssen, B. J., Perry, N. B., Denny, W. A., and Snowden, K. C. (2018) Inhibition of strigolactone receptors by *N*-phenylanthranilic acid derivatives: structural and functional insights. *J. Biol. Chem.* **293,** 6530–6543 CrossRef Medline
31. Tsuchiya, Y., Yoshimura, M., Sato, Y., Kuwata, K., Toh, S., Holbrook-Smith, D., Zhang, H., McCourt, P., Itami, K., Kinoshita, T., and Hagihara, S. (2015) Probing strigolactone receptors in *Striga hermonthica* with fluorescence. *Science* **349,** 864–868 CrossRef Medline
32. Abramyan, T. M., Snyder, J. A., Thyparambil, A. A., Stuart, S. J., and Latour, R. A. (2016) Cluster analysis of molecular simulation trajectories for systems where both conformation and orientation of the sampled states are important. *J. Comp. Chem.* **37,** 1973–1982 CrossRef Medline
33. Phillips, J. L., Colvin, M. E., and Newsam, S. (2011) Validating clustering of molecular dynamics simulations using polymer models. *BMC Bioinformatics* **12,** 445 CrossRef Medline
34. Delaux, P.-M., Xie, X., Timme, R. E., Puech-Pages, V., Dunand, C., Lecompte, E., Delwiche, C. F., Yoneyama, K., Bécard, G., and Séjalon-Delmas, N. (2012) Origin of strigolactones in the green lineage. *New Phytol.* **195,** 857–871 CrossRef Medline
35. Boyer, F.-D., de Saint Germain, A., Pillot, J.-P., Pouvreau, J.-B., Chen, V. X., Ramos, S., Stévenin, A., Simier, P., Delavault, P., Beau, J.-M., and Rameau, C. (2012) Structure-activity relationship studies of strigolactone-related molecules for branching inhibition in garden pea: molecule design for shoot branching. *Plant Physiol.* **159,** 1524–1544 CrossRef Medline
36. Umehara, M., Cao, M., Akiyama, K., Akatsu, T., Seto, Y., Hanada, A., Li, W., Takeda-Kamiya, N., Morimoto, Y., and Yamaguchi, S. (2015) Structural requirements of strigolactones for shoot branching inhibition in rice and *Arabidopsis*. *Plant Cell Physiol.* **56,** 1059–1072 CrossRef Medline
37. Kabsch, W. (2010) XDS. *Acta Crystallogr. D Biol. Crystallogr.* **66,** 125–132 CrossRef
38. Battye, T. G. G., Kontogiannis, L., Johnson, O., Powell, H. R., and Leslie, A. G. W. (2011) iMOSFLM: a new graphical interface for diffraction-image processing with MOSFLM. *Acta Crystallogr. D Biol. Crystallogr.* **67,** 271–281 CrossRef
39. Winn, M. D., Ballard, C. C., Cowtan, K. D., Dodson, E. J., Emsley, P., Evans, P. R., Keegan, R. M., Krissinel, E. B., Leslie, A. G. W., McCoy, A., McNicholas, S. J., Murshudov, G. N., Pannu, N. S., Potterton, E. A., Powell, H. R., Read, R. J., Vagin, A., and Wilson, K. S. (2011) Overview of the CCP4 suite and current developments. *Acta Crystallogr. D Biol. Crystallogr.* **67,** 235–242 CrossRef
40. Evans, P. R. (2011) An introduction to data reduction: space-group determination, scaling and intensity statistics. *Acta Crystallogr. D Biol. Crystallogr.* **67,** 282–292 CrossRef
41. Evans, P. (2006) Scaling and assessment of data quality. *Acta Crystallogr. D Biol. Crystallogr* **62,** 72–82 CrossRef
42. McCoy, A. J. (2007) Solving structures of protein complexes by molecular replacement with Phaser. *Acta Crystallogr. D Biol. Crystallogr.* **63,** 32–41 CrossRef
43. McCoy, A. J., Grosse-Kunstleve, R. W., Adams, P. D., Winn, M. D., Storoni, L. C., and Read, R. J. (2007) Phaser crystallographic software. *J. Appl. Crystallogr.* **40,** 658–674 CrossRef Medline
44. Emsley, P., and Cowtan, K. (2004) Coot: model-building tools for molecular graphics. *Acta Crystallogr. D Biol. Crystallogr.* **60,** 2126–2132 CrossRef
45. Murshudov, G. N., Vagin, A. A., and Dodson, E. J. (1997) Refinement of Macromolecular structures by the maximum-likelihood method. *Acta Crystallogr. D Biol. Crystallogr.* **53,** 240–255 CrossRef
46. Abraham, M. J., Murtola, T., Schulz, R., Páll, S., Smith, J. C., Hess, B., and Lindahl, E. (2015) GROMACS: high performance molecular simulations through multi-level parallelism from laptops to supercomputers. *SoftwareX* **1–2,** 19–25 CrossRef
47. Hornak, V., Abel, R., Okur, A., Strockbine, B., Roitberg, A., and Simmerling, C. (2006) Comparison of multiple Amber force fields and development of improved protein backbone parameters. *Proteins* **65,** 712–725 CrossRef Medline
48. Jorgensen, W. L., Chandrasekhar, J., Madura, J. D., Impey, R. W., and Klein, M. L. (1983) Comparison of simple potential functions for simulating liquid water. *J. Chem. Physics* **79,** 926–935 CrossRef
49. Hess, B., Bekker, H., Berendsen, H. J., and Fraaije, J. G. (1997) LINCS: a linear constraint solver for molecular simulations. *J. Comp. Chem.* **18,** 1463–1472 CrossRef
50. Di Pierro, M., Elber, R., and Leimkuhler, B. (2015) A stochastic algorithm for the isobaric–isothermal ensemble with Ewald summations for all long range forces. *J. Chem. Theory Comput.* **11,** 5624–5637 CrossRef Medline

51. Bussi, G., Donadio, D., and Parrinello, M. (2007) Canonical sampling through velocity rescaling. *J. Chem. Physics* **126,** 014101 CrossRef Medline
52. Berendsen, H. J. C., Postma, J. P. M., Gunsteren, W. F. v., DiNola, A., and Haak, J. R. (1984) Molecular dynamics with coupling to an external bath. *J. Chem. Physics* **81,** 3684–3690 CrossRef
53. Humphrey, W., Dalke, A., and Schulten, K. (1996) VMD: visual molecular dynamics. *J. Mol. Graph.* **14,** 33–38 CrossRef Medline
54. Maier, R., Brandner, C., Hintner, H., Bauer, J., and Onder, K. (2008) Construction of a reading frame-independent yeast two-hybrid vector system for site-specific recombinational cloning and protein interaction screening. *BioTechniques* **45,** 235–244 CrossRef Medline
55. James, P., Halladay, J., and Craig, E. A. (1996) Genomic libraries and a host strain designed for highly efficient two-hybrid selection in yeast. *Genetics* **144,** 1425–1436 Medline